

Numerical Structure Analysis of Regular Hydrogen-Oxygen Detonations

Ralf Deiterding

California Institute of Technology

1200 East California Blvd., MC 158-79, Pasadena, CA 91125

ralf@cacr.caltech.edu

Abstract

Large-scale numerical simulations have been carried out to analyze the internal wave structure of a regular oscillating low-pressure $\text{H}_2 : \text{O}_2 : \text{Ar}$ -Chapman-Jouguet detonation in two and three space-dimensions. The chemical reaction is modeled with a non-equilibrium mechanism that consists of 34 elementary reactions and uses nine thermally perfect gaseous species. A high local resolution is achieved dynamically at run-time by employing a block-oriented adaptive finite volume method that has been parallelized efficiently for massively parallel machines. Based on a highly resolved two-dimensional simulation we analyze the temporal development of the flow field around a triple point during a detonation cell in great detail. In particular, the influence of the reinitiation phase at the beginning of a detonation cell is discussed. Further on, a successful simulation of the cellular structure in three space-dimensions for the same configuration is presented. The calculation reproduces the experimentally observed three-dimensional mode of propagation called “rectangular-mode-in-phase” with zero phase shift between the transverse waves in both space-directions perpendicular to the detonation front and shows the same oscillation period as the two-dimensional case.

1 Introduction

Multi-dimensional detonation waves inherently exhibit non-neglectable instationary sub-structures. The Zel’dovich-von Neumann-Döring (ZND) theory is widely believed to reproduce the one-dimensional detonation structure correctly, but already early experiments [5, 26] uncovered that the reduction to one space dimension is not even justified in long combustion devices. It was found that real detonation waves are usually highly unstable and do not remain planar. The instability manifests itself in instationary shock waves propagating perpendicular to the detonation front. A complex flow pattern is formed around each *triple point*, where the detonation front is intersected by a transverse shock. Some particular mixtures, e.g. low-pressure hydrogen-oxygen with high argon diluent, are known to produce very regular triple point movements. The triple point trajectories form regular “fish-scale” patterns, so called detonation cells, with a characteristic length L and width λ (compare left sketch of Fig. 1).

Fig. 1 displays the hydrodynamic flow pattern of a detonation with regular cellular structure, how it is known since the early 1970th, cf. [25, 18]. The right sketch shows the periodic wave configuration around a triple point in detail. The undisturbed detonation front is called the incident shock, while the transverse wave takes the role of a reflected shock. The triple point is driven forward by a strong shock wave, called Mach stem. Mach stem and reflected shock enclose the slip line, the contact discontinuity.

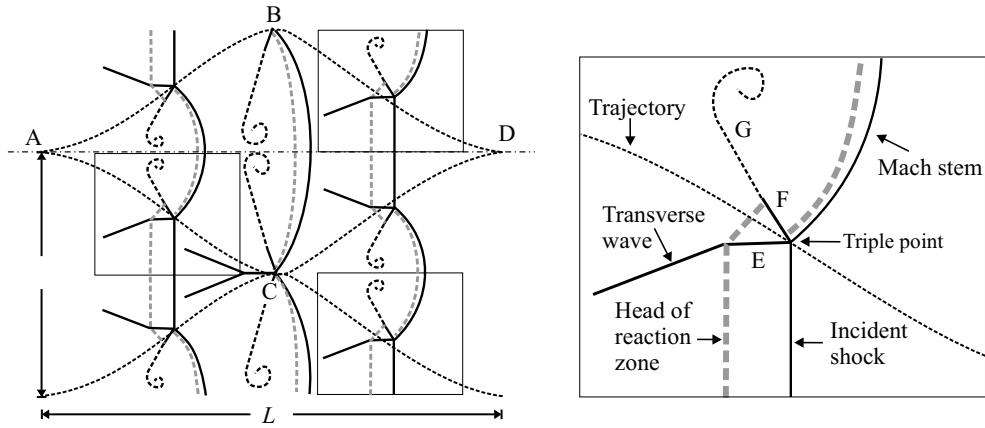


Figure 1: Left: regular detonation structure at three different time steps on triple point trajectories, right: enlargement of a periodical triple point configuration. E: reflected shock, F: slip line, G: diffusive extension of slip line with flow vertex.

The Mach stem is always much stronger than the incident shock, which results in a considerable reduction of the induction length l_{ig} , the distance between leading shock and measurable reaction. The shock front inside the detonation cell travels as two Mach stems from point A to the line BC. In the points B and C the triple point configuration is inverted nearly instantaneously and the front in the cell becomes the incident shock. Along the symmetry line AD the change is smooth and the shock strength decreases continuously. In D the two triple points merge exactly in a single point. The incident shock vanishes completely and the slip line, which was necessary for a stable triple point configuration between Mach stem and incident shock, is torn off and remains behind. Two new triple points with two new slip lines develop immediately after D.

But the experimental analysis of the described transient sub-structures is difficult. Direct numerical simulation of the governing equations can be an alternative here [22, 6, 9, 32].

1.1 Governing equations

An appropriate model for detonation propagation in premixed gases with realistic chemistry are the Euler equations for multiple thermally perfect species with chemically reactive source terms [8, 33]. In d -dimensional Cartesian coordinates these equations can be written as an inhomogeneous conservation law of the structure

$$\frac{\partial}{\partial t} \mathbf{q}(\mathbf{x}, t) + \sum_{n=1}^d \frac{\partial}{\partial x_n} \mathbf{f}_n(\mathbf{q}(\mathbf{x}, t)) = \mathbf{s}(\mathbf{q}(\mathbf{x}, t)). \quad (1)$$

We choose the form

$$\mathbf{q}(\mathbf{x}, t) = (\rho_1, \dots, \rho_K, \rho u_1, \dots, \rho u_d, \rho E)^T, \quad (2)$$

where the partial densities ρ_i sum up to the total density of the mixture $\rho = \sum_{i=1}^K \rho_i$. We denote the n th component of the velocity vector $\mathbf{u} = (u_1, \dots, u_d)^T$ by u_n and E

is the total energy per unit mass. The flux functions are

$$\mathbf{f}_n(\mathbf{q}) = (\rho_1 u_n, \dots, \rho_K u_n, \rho u_1 u_n + \delta_{1n} p, \dots, \rho u_d u_n + \delta_{dn} p, u_n(\rho E + p))^T \quad (3)$$

for $n = 1, \dots, d$. Herein, p is the hydrostatic pressure and δ_{jn} denotes the Kronecker-Symbol. We assume that all species are *thermally perfect* ideal gases in thermal equilibrium. According to Dalton's law the total pressure is then given by

$$p = \sum_{i=1}^K p_i = \mathcal{R}T \sum_{i=1}^K \frac{\rho_i}{W_i}, \quad (4)$$

where the temperature T has to be calculated *iteratively*, whenever the pressure p has to be evaluated. For the vector of state (1) the source terms of detailed chemical reaction take the form

$$\mathbf{s}(\mathbf{q}) = (W_1 \dot{\omega}_1, \dots, W_K \dot{\omega}_K, 0, \dots, 0, 0)^T,$$

where we evaluate the production rates $\dot{\omega}_i$ by usual Arrhenius kinetics [8, 33]. For the simulations throughout this paper only a non-equilibrium hydrogen-oxygen reaction mechanism extracted from a larger hydrocarbon mechanism assembled by Westbrook [31] has been employed. It consists of 34 elementary reactions and uses the nine species H, O, OH, H₂, O₂, H₂O, HO₂, H₂O₂ and Ar.

2 Detonation Simulation

We use the method of fractional steps [12] to decouple hydrodynamic transport and chemical reaction numerically. The homogeneous partial differential equation

$$\mathcal{H}^{(\Delta t)} : \quad \frac{\partial \mathbf{q}}{\partial t} + \sum_{n=1}^d \frac{\partial}{\partial x_n} \mathbf{f}_n(\mathbf{q}) = 0, \quad \text{IC: } \mathbf{Q}^\kappa \xrightarrow{\Delta t} \tilde{\mathbf{Q}}^{\kappa+1} \quad (5)$$

and the usually stiff ordinary differential equation

$$\mathcal{S}^{(\Delta t)} : \quad \frac{\partial \mathbf{q}}{\partial t} = \mathbf{s}(\mathbf{q}), \quad \text{IC: } \tilde{\mathbf{Q}}^{\kappa+1} \xrightarrow{\Delta t} \mathbf{Q}^{\kappa+1} \quad (6)$$

are integrated successively with the discrete data \mathbf{Q} from the preceding step as initial condition (IC).

2.1 Finite Volume Discretization

As the reaction in a detonation wave is induced by a discontinuous hydrodynamic shock wave, we apply the finite volume (FV) approach to discretize (1). For instance, in two-space dimensions a *conservative* time-explicit finite volume scheme for Eq. (5) has the formal structure

$$\mathcal{H}^{(\Delta t)} : \quad \tilde{\mathbf{Q}}_{jk}^{\kappa+1} = \mathbf{Q}_{jk}^\kappa - \frac{\Delta t}{\Delta x_1} \left[\mathbf{F}_{j+\frac{1}{2},k}^1 - \mathbf{F}_{j-\frac{1}{2},k}^1 \right] - \frac{\Delta t}{\Delta x_2} \left[\mathbf{F}_{j,k+\frac{1}{2}}^2 - \mathbf{F}_{j,k-\frac{1}{2}}^2 \right]. \quad (7)$$

Such a scheme can easily be constructed by applying the idea of operator splitting also to Eq. (5) and by using two quasi-one-dimensional FV schemes successively, i.e. $\mathcal{H}^{(\Delta t)} = \mathcal{X}_2^{(\Delta t)} \mathcal{X}_1^{(\Delta t)}$. With this definition the entire splitting method reads $\mathbf{Q}^{\kappa+1} = \mathcal{S}^{(\Delta t)} \mathcal{X}_2^{(\Delta t)} \mathcal{X}_1^{(\Delta t)}(\mathbf{Q}^\kappa)$. The later method is only formally first-order accurate, but it usually gives very satisfactory results, if high-resolution shock-capturing schemes are employed for the operators $\mathcal{X}_n^{(\Delta t)}$. Formally second-order accurate splitting methods are possible [29], but we have observed only minor improvements for detonation structure simulations like those presented in the Secs. 3 and 4.

2.2 High-resolution Upwind Method

The operators $\mathcal{X}_n^{(\Delta t)}$ can be implemented effectively with a single quasi-one-dimensional scheme that allows the canonical exchange of the velocities u_n and the indices j and k . Our high-resolution scheme uses the second-order MUSCL-Hancock variable extrapolation technique by Van Leer [30] and is built around a first-order Godunov-type method that solves the Riemann problem between two neighboring cell values \mathbf{Q}_l and \mathbf{Q}_r approximately. The method is based on an extension of Roe’s linearized Riemann solver for Euler equations for a single polytropic gas for multiple thermally perfect species by Grossman and Cinella [10]. The intrinsic problem of unphysical total densities and internal energies near vacuum due to the Roe linearization [7] is circumvented by switching in case of an physical approximation to the simple, but extremely robust Harten-Lax-Van Leer (HLL) Riemann solver. Negative mass fraction values are avoided by a numerical flux modification proposed by Larrourou [17]. Finally, the occurrence of the disastrous carbuncle phenomena, a multi-dimensional numerical crossflow instability that destroys every simulation of strong grid-aligned shocks or detonation waves completely [23], is prevented by introducing a small amount of additional numerical viscosity in a multi-dimensional way [24]. A detailed derivation of the entire Roe-HLL scheme including all necessary modifications can be found in [3].

2.3 Integration of Reaction Terms

The numerical treatment of chemical reaction terms with the method of fractional steps requires the solution of the stiff ordinary differential equations in every FV cell. For this purpose we employ a semi-implicit Rosenbrock-Wanner method by Kaps and Rentrop of fourth order with automatic step-size adjustment [14]. The computational expensive reaction rates $\dot{\omega}_i$ are evaluated by a mechanism-specific routine, which is produced by a source code generator on top of the Chemkin-II library [15] in advance.

2.4 Evaluation of the Temperature

The FV method for thermally perfect gas-mixtures sketched in Sec. 2.2 and the reaction term integration described in the previous section require the iterative compu-

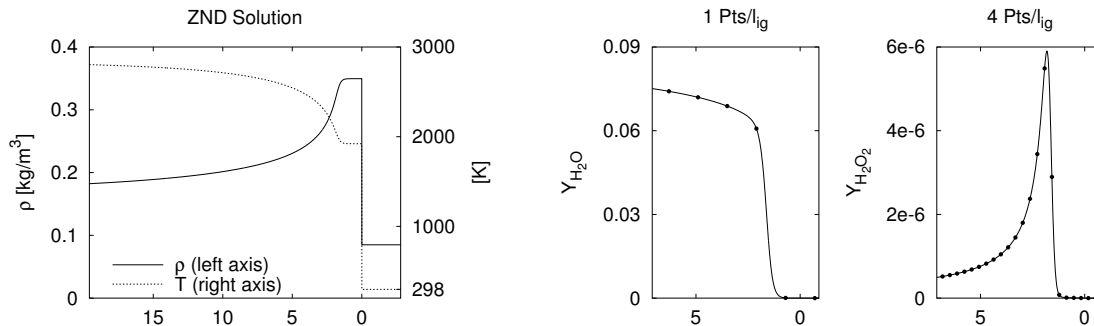


Figure 2: A self-sustaining hydrogen-oxygen detonation ($d_{CJ} \approx 1627$ m/s, $l_{ig} \approx 1.404$ mm) calculated with the ZND theory and representation of two mass fraction distributions on grids with different mesh widths (right). The dots represent the values in the center of a finite volume. The abscissas display the distance behind the detonation front in mm.

tation of the temperature T from a discrete vector of state \mathbf{Q} . We start the solution procedure with a standard Newton iteration that is initialized with the temperature value of the preceding time step. If the Newton method does not converge in a reasonable number of steps, a standard bisection technique is employed.

In order to speed up further the polynomial evaluation of temperature-dependent transport properties, look-up tables for all species are constructed during the startup of the computational code. These tables store the values according to the usual polynomial approximation [27, 16] for all integers in the valid temperature range and intermediate values are interpolated.

2.5 Meshes for Detonation Simulation

Numerical simulations of detonation waves require computational meshes, which are able to represent the strong local flow changes due to the reaction correctly. In particular, the shock of a detonation wave with detailed kinetics can be very sensitive to changes of the reaction behind and, if the mesh is too coarse to resolve all reaction details correctly, the Riemann Problem at the detonation front is changed remarkably leading to a wrong speed of propagation. We make a simple discretization test in order to illustrate, how fine computational meshes for accurate detonation simulations in fact have to be. The left graph of Fig. 2 displays the flow fields of ρ and T according to the ZND detonation model for the frequently studied $\text{H}_2 : \text{O}_2 : \text{Ar}$ CJ detonation with molar ratios $2 : 1 : 7$ at $T_0 = 298$ K and $p_0 = 6.67$ kPa.

The two left graphs of Fig. 2 display the *exact* distributions of $Y_{\text{H}_2\text{O}}$ and $Y_{\text{H}_2\text{O}_2}$ discretized with different FV grids. Apparently, a resolution of 4 finite volumes per induction length ($4 \text{ Pts}/l_{ig}$) is not sufficient to capture the maximum of the intermediate product H_2O_2 correctly. This requires at least 5 to 6 Pts/l_{ig} , but in triple points even finer resolutions can be expected. The discretization of typical combustors with such fine uniform grids can easily require up to 10^9 FV cells in the two- and up to 10^{12} cells in the three-dimensional case. As multi-dimensional detonations

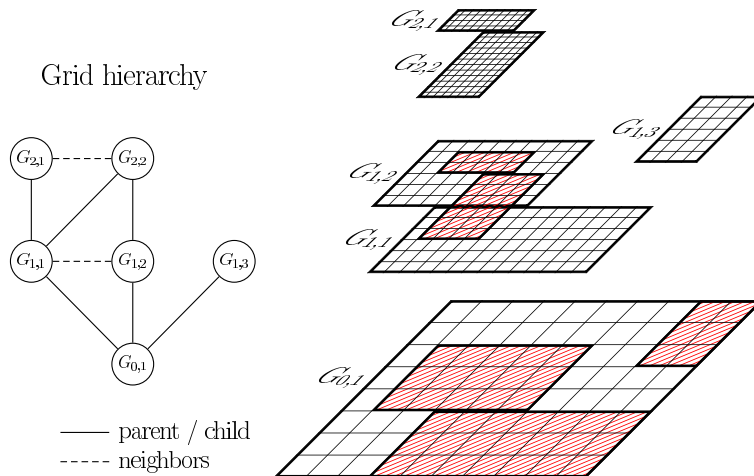


Figure 3: The AMR method creates a hierarchy of rectangular subgrids.

are intrinsically unstable (compare Sec. 1), numerical simulations have to be stationary and usually involve several ten thousand time steps. Consequently, uniform meshes are far too expensive and the application of a sophisticated dynamically adaptive mesh refinement technique is indispensable.

2.6 Adaptive Mesh Refinement

In order to supply the required temporal and spatial resolution efficiently, we employ the blockstructured adaptive mesh refinement (AMR) method after Berger and Colella [2], which is tailored especially for hyperbolic conservation laws on logically rectangular FV grids (not necessarily Cartesian).

Instead of replacing single cells by finer ones, as it is done in cell-oriented refinement techniques, the Berger-Colella AMR method follows a patch-oriented approach. Cells being flagged by various error indicators (shaded in Fig. 3) are clustered with a special algorithm [1] into non-overlapping rectangular grids with identical refinement factor on each level. Refinement grids are derived recursively from coarser ones and a hierarchy of successively embedded levels is thereby constructed, cf. Fig. 3.

The numerical scheme is applied on each level by calling the single-grid routines $\mathcal{H}^{(\Delta t)}$, $\mathcal{S}^{(\Delta t)}$ in a loop over all subgrids. The method is usually implemented with ghost or halo cells to implement physical boundary conditions and, if all ghost cells on a level are set appropriately, the update sweep over the subgrids can be done in parallel. Inefficient small subgrids are effectively avoided by leaving coarse level data structures untouched, when higher level grids are created. Values of cells covered by finer subgrids are overwritten by averaged fine grid values subsequently.

We have implemented the AMR method in a generic, dimension-independent object-oriented framework in C++. It is called AMROC (Adaptive Mesh Refinement in Object-oriented C++) and is free of charge for scientific use [4]. The framework follows a locality-preserving parallelization strategy, which is based on

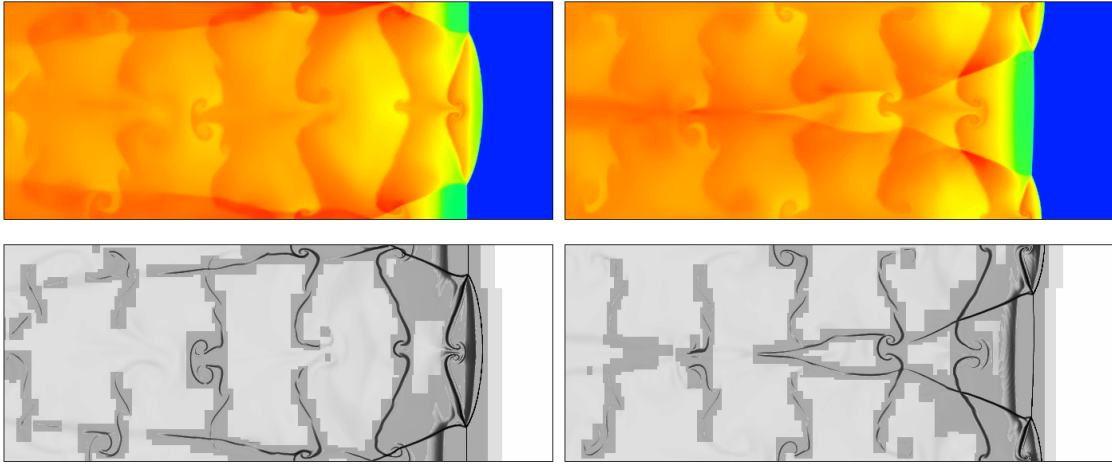


Figure 4: Color plots of the temperature (upper row) and schlieren plots of the density on refinement regions in the first (left) and second half (right) of a detonation cell.

rigorous domain decomposition and partitions the entire AMR hierarchy from the base level. The implementation relies on the MPI-library and is therefore tailored especially for the emerging generation of distributed memory machines, e.g. for Linux-Beowulf-clusters.

3 Two-dimensional Cellular Structure

The self-sustaining Chapman-Jouguet (CJ) detonation discussed in Sec. 2.5 is known experimentally [25] to produce very regular detonation cells in multiple space-dimensions. Hence, it is an ideal candidate for fundamental detonation structure simulations and especially the early computations with one- or two-step reaction models were done for this system [28, 13, 20, 21].

The first successful two-dimensional detonation structure simulation with detailed non-equilibrium chemistry was presented by Oran and her collaborators in [22]. To reduce the extraordinary costs on uniform meshes, Geßner [9] and Eckett [6] studied this particular configuration with different mesh adaptation techniques, but were unable to achieve better resolved results, because no parallel simulation codes were employed. The AMROC framework allowed the computation of a new reference solution with an increase of spatial resolution compared to all published results [22, 9, 6] by a factor > 4.5 in both space dimensions.

3.1 Computational Setups and Initialization

We extend the one-dimensional ZND detonation of Fig. 2 to two space dimensions with $u_2 = 0$ and initiate transverse disturbances by placing a small rectangular unreacted pocket with the temperature 2086 K behind the detonation front, cf. [22]

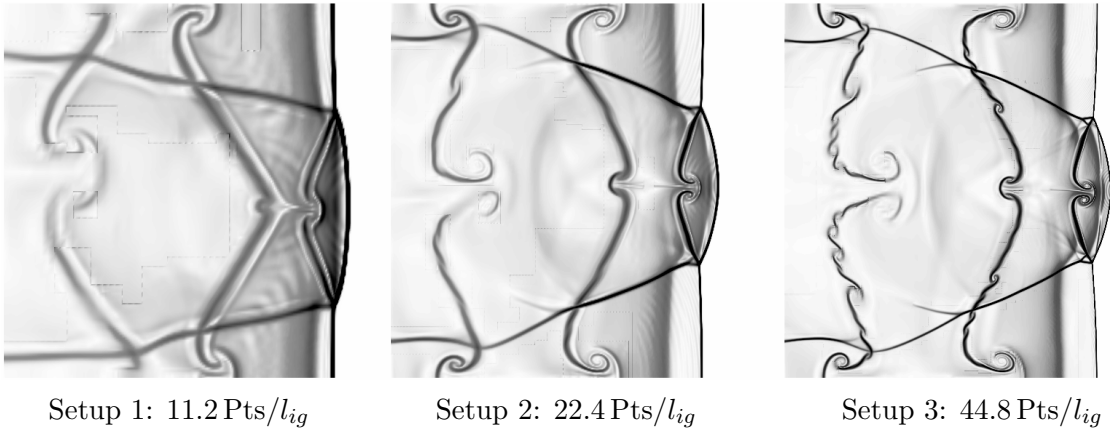


Figure 5: Schlieren plots of T for the three computational setups.

or [3]. After an initial period of $\approx 200 \mu\text{s}$ very regular detonation cells with $\lambda \approx 3 \text{ cm}$ show up. We exploit this regularity and simulate only a single cell. The calculation is done in a frame of reference attached to the detonation and requires just the computational domain $10 \text{ cm} \times 3 \text{ cm}$.

We utilize the three different adaptive setups of Tab. 1 with the resolutions 11.2, 22.4 and 44.8 Pts/ l_{ig} on the finest level to study the convergence of the solution and to obtain highly resolved reference results. All computations end at $t_{end} = 800 \mu\text{s}$, where automatic time step adjustment based on $C_{CFL} \approx 0.95$ was applied. A physically motivated combination of scaled gradients and heuristically estimated relative errors is applied as adaptation criteria. See [3] for details.

Setup	Base grid	r_1	r_2	Pts/ l_{ig}
1	100×20	2	4	11.2
2	100×20	4	4	22.4
3	200×40	4	4	44.8

Table 1: Base grid and refinement factors of the three different setups.

3.2 Comparison of the Computational Results

The Setups 1 to 3 lead to basically similar numerical results. The oscillation period t_p ranges from $\approx 31.3 \mu\text{s}$ for Setup 1 to $\approx 32.5 \mu\text{s}$ for Setup 3, which corresponds to an increase of the cell length L from $\approx 5.1 \text{ cm}$ to $\approx 5.3 \text{ cm}$ as the grid is refined. Further on, the triple point tracks (not shown) appear to be more curved with increasing resolution.

A comparison of typical schlieren plots of relevant flow quantities for all three setups is presented in Fig. 5. While the results of the coarsest computation only allow the distinction of the discontinuities of the basic triple point structure visualized in Fig. 1, the results of Setup 2 and especially of Setup 3 show important sub-structures. In particular, a secondary triple point can clearly be distinguished along the transverse wave.

The dynamic adaptation is qualitatively similar in all computations. Two typical situations in the first and the second half of a detonation cell are displayed in Fig. 4. In case of Setup 1 the adaptive computation uses about 36,000 cells instead of

128,000 cells (uniform refinement). Setup 3 uses between 340,000 and 390,000 cells instead of 2,048,000. A breakdown of the computational time spent in the computationally most expensive parts of the code for this setup is given in Tab. 2. The numerical integration is split into the two main steps of the fractional step method: the homogeneous fluid dynamic update and the integration of the reactive source term. A ratio between these portions of 1.1 is in good agreement with timings reported in [22] and underlines that we achieve a reasonable load-balancing without considering the number of sub-cycling time steps in the source term integration in the workload estimation explicitly. The third important portion in Tab. 2 is the time for setting the ghost cell values, which is dominated ($\approx 90\%$) by parallel communication for synchronization.

Task	%
Fluid dynamics	33.5
Chemical kinetics	36.8
Boundary setting	26.8
Recomposition	2.4
Misc.	0.5
Total [h CPU]	2150

Table 2: Breakdown of computing time for Setup 3.

3.3 Flow Features of the Oscillating Solution

The highly resolved results of Setup 3 uncover a flow structure in the vicinity of a triple point that is remarkably more complex than the basic flow field shown in Fig. 1. The first refinement of the basic flow interpretation for low-pressure $\text{H}_2 : \text{O}_2$ CJ detonations was given by Lefebvre and Oran in [19] utilizing a two-step reaction model and extended (at least partially) to detailed chemistry in [22]. As the two transverse waves form a perfectly regular hydrodynamic flow that is reproduced almost identically after $t_p \approx 32.5 \mu\text{s}$, cf. Figs. 15 and 16, it suffices to study a single triple point between two triple point collisions.

3.3.1 Triple Point Structure Before a Collision

We start our presentation of the detailed triple point flow structure with the situation that is mostly preserved in Setup 3 from the simulated time $t = 630 \mu\text{s}$ until the collision at $t = 636.25 \mu\text{s}$. Fig. 6 uncovers the existence of two minor triple points B and C along the transverse wave downstream of A. While B can be clearly identified by a characteristic inflection, the triple point C is much weaker and very diffused. B is caused by the interaction of the strong shock wave BD with the transverse wave. The slip line emanating from B to K is clearly present. C seems to be caused by the reaction front (which can be interpreted as a diffused contact discontinuity) and generates the very weak shock wave CI. Downstream of BD a weaker shock wave EF shows up. It is refracted in the point F, when it hits the slip line BK. From F to G this minor shock is parallel and close to the transverse wave, which results in a higher pressure increase in the region FG than in the region EF. Unreacted gas crossing the transverse wave between B and C therefore shows a shorter induction length than gas entering through AB. The minor shock is refracted and weakened by the reaction front at point G and forms the shock GH that is almost parallel to CI.

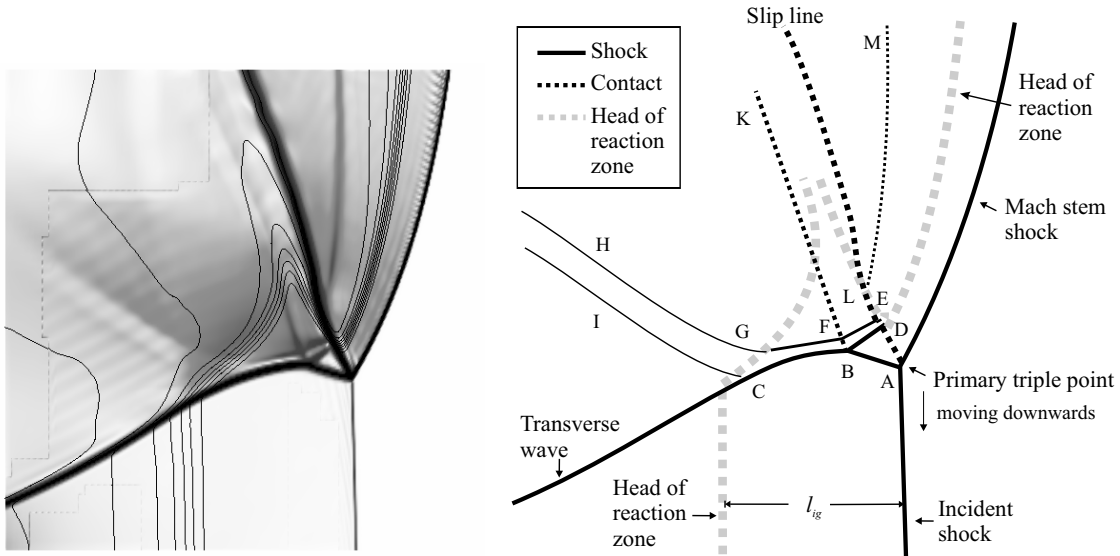


Figure 6: Flow structure around a triple before the next collision. Left: isolines of Y_{OH} (black) on schlieren plot of u_2 (gray).

The downstream line of separation between particles passing through incident or Mach Stem shock is the slip line AD. Along its extension DEL the movement of A results in a shear flow between the reaction zones behind the Mach stem and downstream of BD. In the actual picture the contact discontinuity LM seems to originate in this shear flow region, but in fact it is only a relict of the reinitiation phase and propagates constantly downstream. It has been caused by the interaction of a shock wave produced by the burning of an unreacted region during the reinitiation phase with the Mach stem shock (see below).

3.3.2 Temporal Development of the Triple Point Structure

The flow pattern described in the previous subsection develops out of the reinitiation after the triple point collision at $t = 620.4 \mu s$ in a time of about $10 \mu s$. This complex flow process is shown in the schlieren plot of the Figs. 17 and schematically sketched in the graphics of the Figs. 7 and 8.

When the two triple points A hit at $t = 620.4 \mu s$ in one single point, the stable configurations around both triple points break down and the old slip lines are torn off immediately. They start to propagate downstream and after the merging of both points D at $t \approx 620.8 \mu s$ they travel as one contact discontinuity. At the same time the new Mach stem is initiated in a point-wise fashion. The temperature behind this new Mach stem is drastically higher than the temperature behind the old Mach stem before the collision. It increases rapidly from $\approx 2500 \text{ K}$ at $t = 619.6 \mu s$ to more than 3500 K at $t = 621.6 \mu s$.

The reinitiation separates the combustion zone behind the leading shock waves from the reaction regions downstream of the transverse wave. An unreacted region forms. It is bounded to the right by the old slip lines, cf. $t = 621.2 \mu s$ in Fig. 7. Its

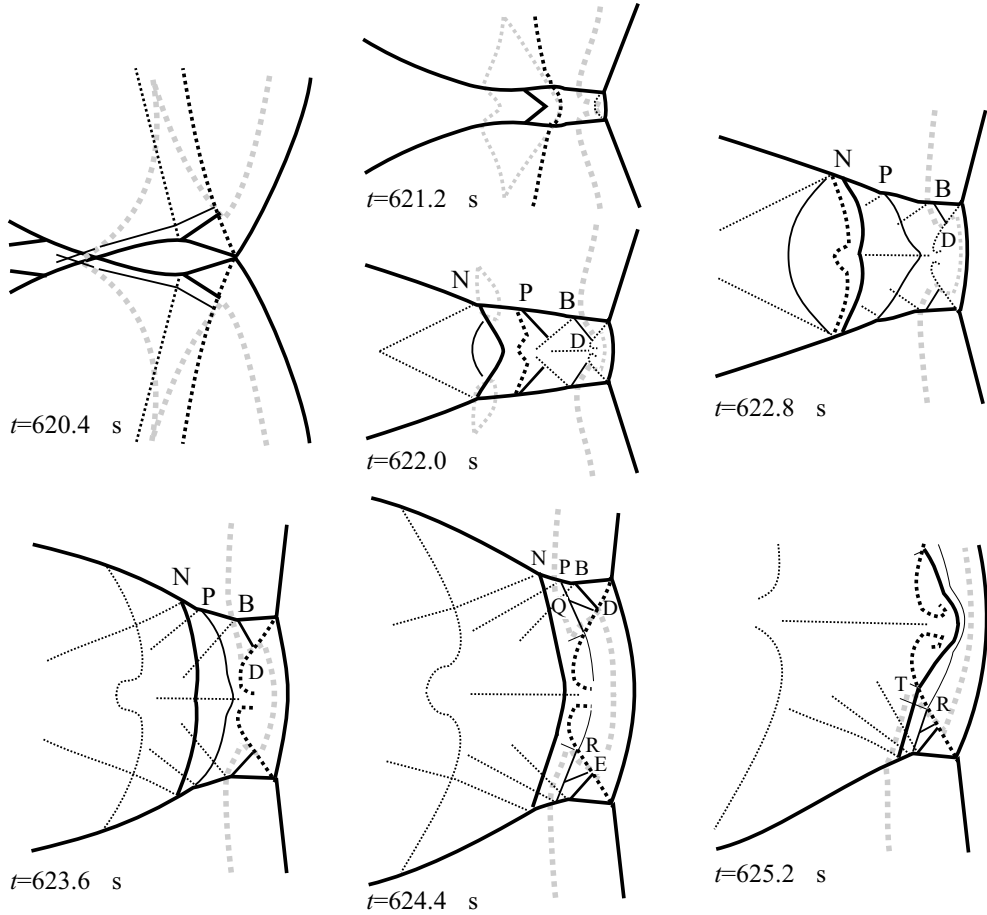


Figure 7: Collision of triple points and development of the double Mach structure.

burning generates shock waves that hit the transverse waves in minor triple points N and P. At $t = 622.0 \mu\text{s}$ two shocks emanating in the upstream direction are visible. Further on, a thorough analysis of the time step $t = 622.0 \mu\text{s}$ uncovers that the secondary triple point B and its shock wave BD are already present. This is very much earlier than it was found in [19]. It is therefore reasonable to assume that the triple point B is inherently connected to the primary triple point A and that only the limited resolution prevents its appearance in the simulation at an earlier stage.

At $t = 624.4 \mu\text{s}$ both shock waves spreading out from the unreacted region have passed the old slip line and the first shock interacts with the new slip lines. It is refracted slightly and very weak triple points R are formed on the new slip lines. Further on, the minor shock emanating from E can be distinguished. Its refraction on the slip line of B can not be observed yet, because the shock forms a weak triple point Q with the shock wave PR. In the next time step also the stronger second shock reaches the new slip lines and forms the triple point T. The triple points Q, R and T are so weak that no corresponding slip lines can be observed at this resolution. The upstream velocity of the stronger shock NT is higher than that of PR and at $t = 626.0 \mu\text{s}$ NT has caught up with PR and strengthens it, compare $t = 626.0 \mu\text{s}$ of Fig. 8. The triple point R is overrun by T. At $t = 626.8 \mu\text{s}$ NT has merged

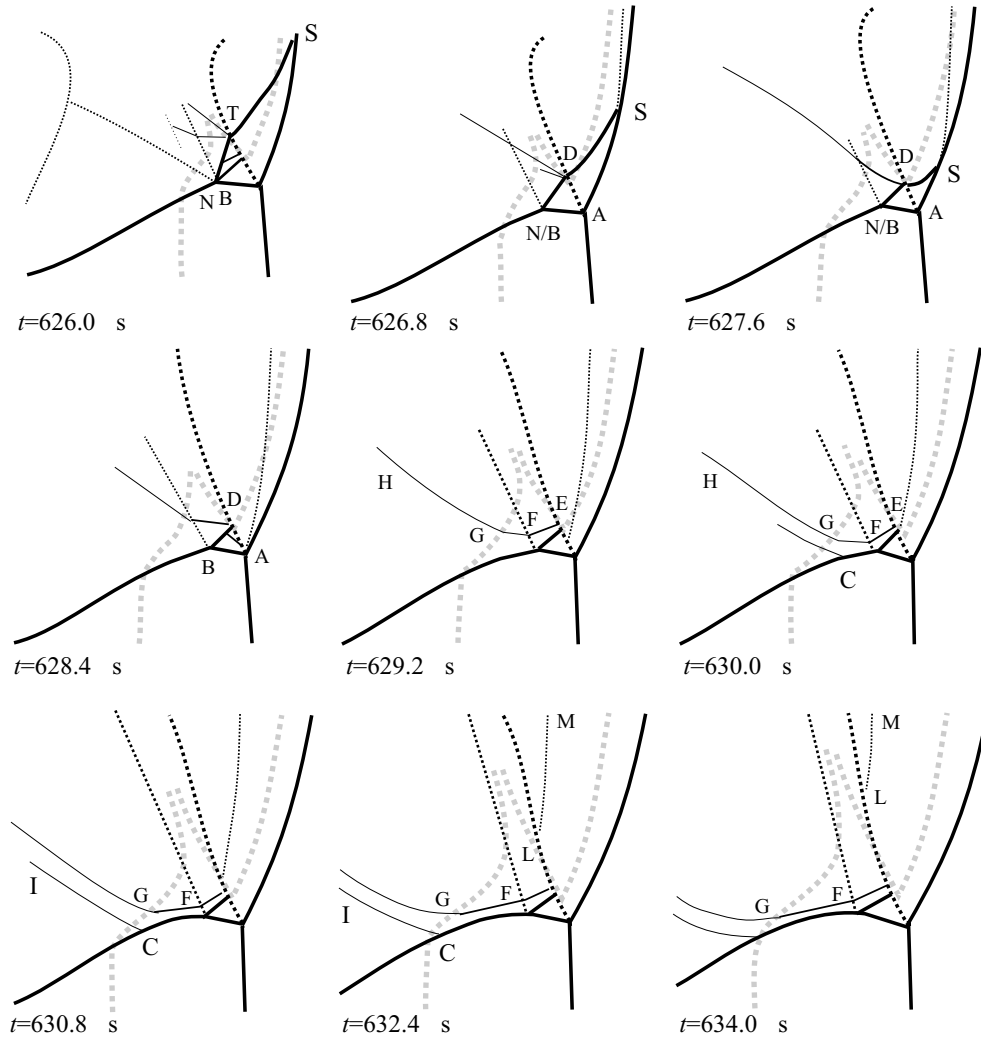


Figure 8: Development of the triple Mach structure out of the double Mach structure before the next collision.

with BD and the shock wave EQ has vanished completely during the passage of NT . The shock wave NT forms a triple point S where it hits the Mach stem. The contact discontinuity emanating from S is clearly visible. In the following, the shock NTS propagates even through the area $ABDS$ and finally reaches the primary triple point A at $t = 628.4 \mu s$. At $t = 628.4 \mu s$ this shock has vanished completely above the slip line AD , only below AD a minor pressure wave has been preserved. Also the minor shock behind BD has reappeared at this time. From $t = 629.2 \mu s$ on the double refraction of this minor shock at F and G can be clearly observed. During the following time steps FG approaches the transverse wave and becomes tangential. The diffusive triple point C is observed first at $t = 630.0 \mu s$. It seems to appear upstream of the reaction front at first, but merges with the beginning of the combustion region subsequently. The contact discontinuity LM , which has been created originally in the triple point S , propagates constantly downstream bounded by the primary slip line.

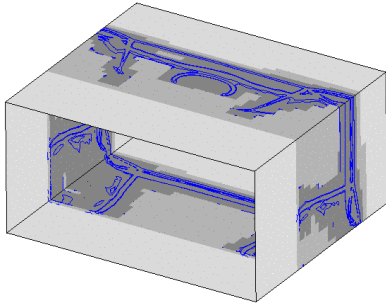


Figure 9: Detonation structure on refinement grids. $4.5 \text{ cm} < x_1 < 7.0 \text{ cm}$.

Task	%
Fluid dynamics	36.7
Chemical kinetics	20.3
Boundary setting	38.4
Recomposition	1.9
Misc.	2.7
Total [h CPU]	3800

Table 3: Breakdown of the computational time for the 3D simulation.

4 Three-dimensional Cellular Structure

We utilize the regular oscillating solution of the preceding section as initial condition for the three-dimensional simulation and disturb the oscillation in the x_2 -direction with an unreacted pocket in the orthogonal direction. We use a computational domain of the size $[0 \text{ cm}, 7 \text{ cm}] \times [0 \text{ cm}, 1.5 \text{ cm}] \times [0 \text{ cm}, 3 \text{ cm}]$ that exploits the symmetry of the initial data in the x_2 -direction, but allows the development of a full detonation cell in the x_3 -direction. The adaptive computation uses a two-level refinement with $r_1 = 2$ and $r_2 = 3$ on a base grid of $140 \times 12 \times 24$ cells (cf. Fig. 9) and utilizes between 1.3 M and 1.5 M cells, instead of 8.7 M cells like a uniformly refined grid. Tab. 3 clearly reflects the increased expense in solving the hydrodynamic equations in three space-dimensions (3431 root level time steps with $C_{CFL} \approx 0.95$ to $t_{end} = 800 \mu\text{s}$).

4.1 Flow Features of the Solution

After a simulation time of $\approx 600 \mu\text{s}$ a regular cellular oscillation with identical strength in x_2 - and x_3 -direction can be observed. In both transverse directions the strong two-dimensional oscillations is present and forces the creation of rectangular detonation cells of 3 cm width. Like in the two-dimensional case the oscillation period is $\approx 32 \mu\text{s}$. The transverse waves form triple point lines in three space-dimensions. During a complete detonation cell the four lines remain mostly parallel to the boundary and hardly disturb each other, cf. Fig. 18. The characteristic triple point pattern can be observed in all planes perpendicular to a triple point line. Each triple point line is driven forward by a Mach stem line into an incident shock region. A region that is a Mach stem in one direction can be either a Mach stem or an incident shock in the orthogonal direction. The same is true for the incident shock and we consequently have three different types of rectangular shock regions at the detonation front: Mach stem - Mach stem (MM), Incident - Incident (II) and mixed type regions (MI) [32]. An MM region is bounded only by Mach stems and expands in x_2 - and x_3 -direction. An II rectangle is formed only by incident shocks and shrinks in both directions. The MI region is of mixed type and expands in one direction, while it shrinks in the other. Fig. 10 displays the different rectangular shock regions

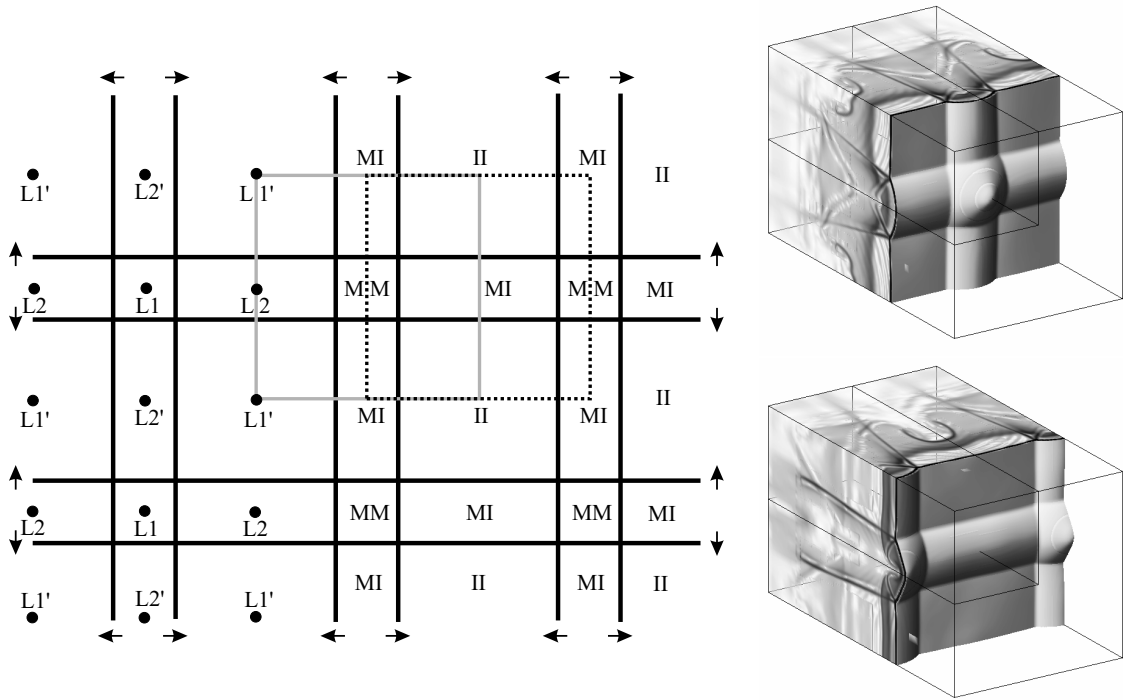


Figure 10: Schematic front view of the periodic triple point line structure. The gray square shows the situation of the upper right plot, the black dotted square corresponds to the lower right plot at the same time.

for a specific snapshot. Apparently, the triple point lines in the upper right or lower right graphic are just periodically shifted by $x_3 = 1.5$ cm. It depends on the initial flow field, which of the displayed situation appears in the simulation at a given time. The equivalence of two computations can also be seen, if the three-dimensional triple point track of one calculation is bisected at $x_3 = 1.5$ cm and mirrored at $x_3 = 0$ cm. Beside a temporal shift the result is de facto identical of the other computation, cf. Fig. 11.

Unlike Williams et al. [32] who presented a similar calculation for an overdriven detonation with simplified one-step reaction model, we notice no phase-shift between both transverse directions. In all our computations for the hydrogen-oxygen CJ detonation only this regular three-dimensional mode, called “rectangular-mode-in-phase” [11], or a purely two-dimensional mode with triple point lines just in x_2 - or x_3 -direction did occur.

4.1.1 Three-dimensional Regular Oscillation

In order to compare the regular oscillations in the two- and three-dimensional case quantitatively, we monitor the temporal development of the detonation velocity along specially selected lines perpendicular to the x_2 - x_3 -plane. These lines are displayed in topview in the left part of Fig. 10. Fig. 11 also displays some exemplary side views. At the beginning of a new detonation cell stands a point-wise reinitiation, when the four triple point lines bounding an II-square merge exactly in a

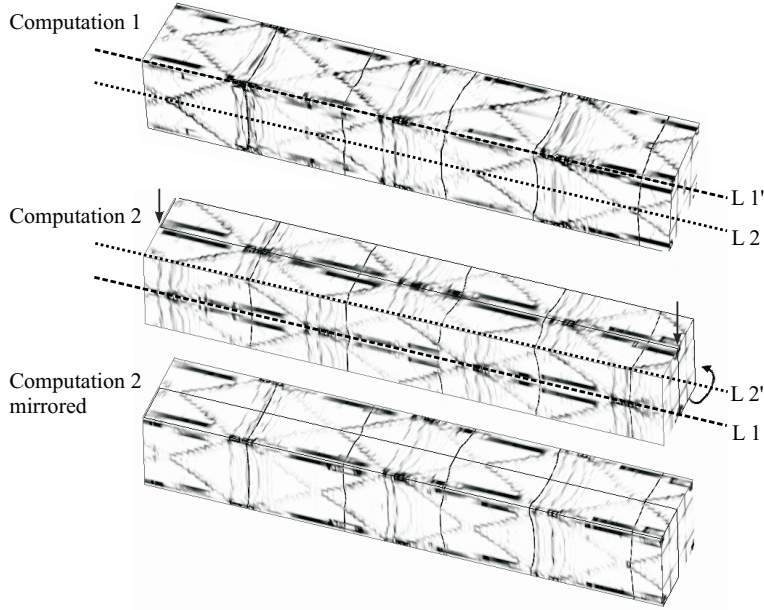


Figure 11: Top and middle: regular triple point tracks in two computations starting from different initial data. Bottom: Bisecting the middle domain at $x_3 = 1.5$ cm and mirroring it at $x_3 = 0$ cm gives triple point tracks that are de facto identical to upper ones.

single point. Because of the regularity of the oscillation these points lie all along lines L1 and L1'. The time between the reinitiation on L1 and L1' is exactly a half oscillation period (compare Fig. 13). After the reinitiation the four triple point lines are diverging and the former II-sector has become an MM-square. A line-wise reinitiation occurs when the converging two triple point lines of an MI-rectangle merge in a single line. Beside L1 and L1' a merging of triple point lines in both transverse directions occurs only along the lines L2 and L2' that pass through the center of the MI-rectangles. The time between the intersection of two triple point lines on L2 or L2' is a half oscillation period (compare Fig. 13).

Fig. 12 displays the temporal development of the detonation velocity relative to the detonation velocity d_{CJ} along the lines L1 and L2. The time period between two cell reinitiations along L1 is $\approx 31.7 \mu\text{s}$. This estimate is in good agreement with our two-dimensional measurements in Sec. 3.2 and corresponds exactly to the oscillation time that can be expected for our numerical method for $16.8 \text{ Pts}/l_{ig}$. The result clearly underlines that the basic two-dimensional instability is exactly preserved in three dimensions, although its manifestation in the hydrodynamic flow field is different. In particular, a direct comparison of the graphs in the two- and three-dimensional case in Fig. 12 uncovers that the three-dimensional detonation is significantly higher overdriven in the reinitiation points of the detonation cells than in the two-dimensional case. On the other hand, the line-wise reinitiation along L2 or L2' involves a considerably less overdriven detonation. It is interesting to

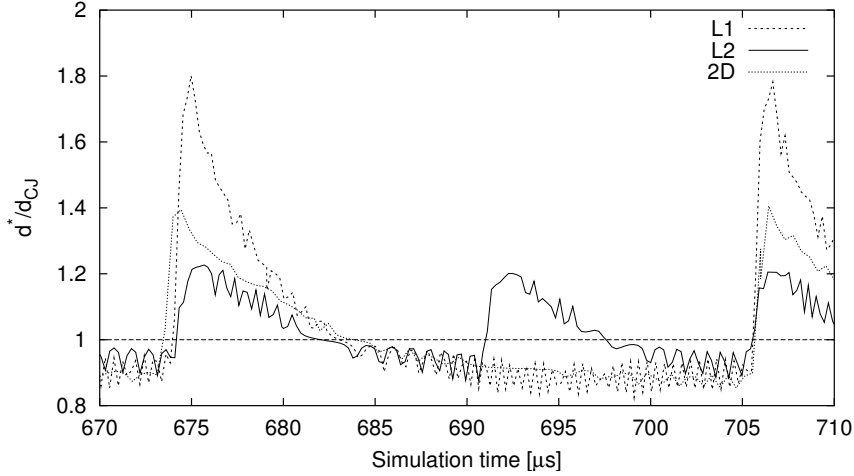


Figure 12: Temporal development of the detonation velocity along the lines L1 and L2 compared to the result of a purely two-dimensional simulation from Sec. 3.

note, that the minimal overdrive factor throughout a detonation cell seems to be independent of the dimension.

The development of the three-dimensional flow field in the one detonation cell completely covered by Fig. 12 is displayed in the Figs. 18 and 19. While the graphics of the left column display schlieren plots of ρ , the right column shows schlieren plots of the mass fraction $Y_{\text{OH}} = \rho_{\text{OH}}/\rho$ overlaid by a transparent blue isosurface of the density. The distance between this isosurface and the gray isosurface of Y_{OH} behind it visualizes the induction distance l_{ig} in the three-dimensional case.

The detonation cell is reinitiated on L1 at $t \approx 675 \mu\text{s}$. Fig. 18 shows the first half of the detonation cell, when L1 is in the center of the MM-square. The graphics clearly reflect the enormous decrease of the induction length immediately after the reinitialization due to the high overdrive factor by the merging of orthogonal triple point lines in the MM-region. The high overdrive factor also changes the appearance of the transverse waves. While the triple point line acts as a diverging boundary of an MM-square on the one side, it is a converging boundary of an II-region on the other. A careful comparison of a cut through the center of Fig. 18 with the side-cuts uncovers that the transverse waves of the same triple point line form very different angles with their corresponding incident shock region. For instance for the time step $t \approx 680 \mu\text{s}$

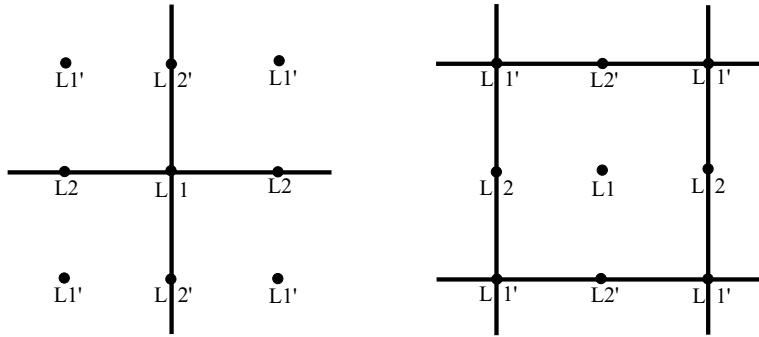


Figure 13: Point-wise reinitiation along L1 (left) and L1' (right). The time between both flow situations is exactly a half oscillation period.

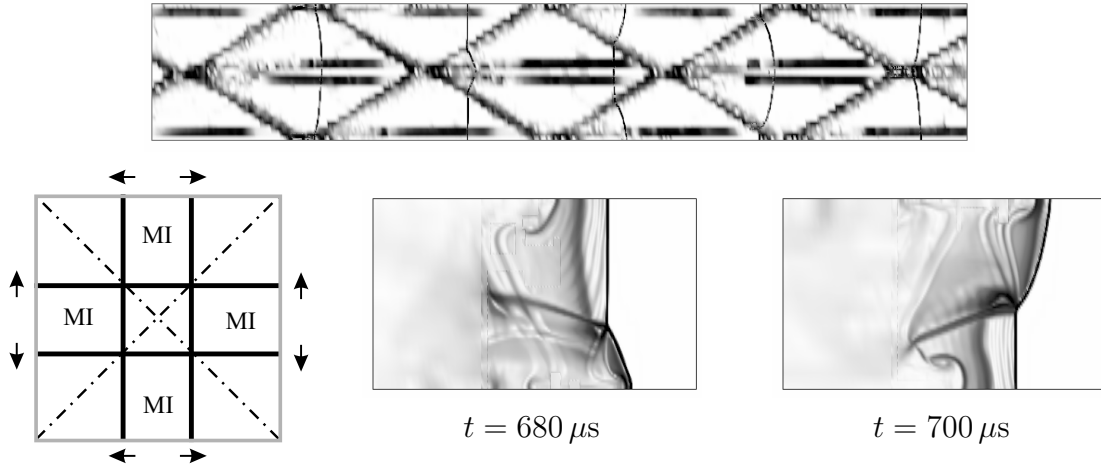


Figure 14: Top: Triple point tracks along a diagonal cut, mirrored at $x_2 = 0$ cm. Bottom, left: cutting planes shown on front view of triple point line structure at $t = 680 \mu s$. Bottom, middle and right: schlieren plots of ρ for one half of 2nd and 3rd detonation front displayed on upper triple point track.

the angle between transverse wave and plane II-shock is approximately 24° , but the angle between transverse wave and MI-shock is only $\approx 10^\circ$. Nevertheless, the propagation velocity of the triple point lines is equal everywhere. This observation is a strong indication that the transverse waves are only the result of the triple point lines. The triple point lines by themselves seem to be the fluid dynamical manifestation of a general oscillation mechanism. Their actual geometry seems to be determined just by the shape of the surrounding combustion chamber.

The development of the detonation front in the second half of a detonation cell is shown in Fig. 19. Especially the right 3D graphic for $t = 704 \mu s$ clearly displays the formation of unreacted regions similar to the one analyzed in the two-dimensional case. In three space-dimensions a deep unreacted region is formed by the four converging triple point lines of the II-square, shallower oblong unreacted regions are developed through the merging of two triple point lines in the MI-regions. The schlieren plot of Y_{OH} at $t = 690.4 \mu s$ displays the formation of the deep unreacted region along L1' and the simultaneous closing of the oblong unreacted regions.

Analogously to the two-dimensional case, the merging of two triple point lines in a single line causes a temporary breakdown of the stable triple point configuration. In particular, the old slip lines are torn off from the detonation front and remain behind. These slip lines have the usual shape along planes perpendicular to a particular triple point line, but they appear as almost straight lines on planes orthogonal to the triple point lines' vector of motion. The time steps $t \geq 696 \mu s$ of Fig. 19 display the downstream propagation of slip lines that have been torn off from the detonation front in the slapping of the triple point lines at the boundary at $t \approx 691 \mu s$.

Finally, we note that regular two-dimensional detonation cells can also be found along the two diagonal cuts going through the middle axis of the computational domain. A diagonal cut through the triple point tracks and diagonal schlieren plots

of the density are displayed in Fig. 14. The detonation cells shown in Fig. 14 have the same length as for example in Fig. 11, but the height is $\lambda = 3\sqrt{2}$ cm. The schlieren plots display the basic triple point pattern. It is interesting to note, that the measurable angle between transverse wave and incident shock in the four points, where II- and MM-region abut directly, is approximately 18° at $t = 680 \mu\text{s}$ and therefore between the two previously measured angles. This indicates that the angle of the transverse waves to the detonation front depends more on the absolute strength of the Mach stem than on the differences between Mach stem and incident shock.

5 Conclusions

We have presented accurate numerical simulations of regularly oscillating hydrogen-oxygen detonations in open space in two- and three space-dimensions. All temporal and spatial scales relevant for the complex process of detonation propagation were successfully resolved and the achieved resolutions are significantly finer than in previous publications [22, 6, 9]. The regular oscillation observed in the three-dimensional case is de facto identical to the two-dimensional case, although its manifestation in the flow field involves a remarkably higher overdrive factor in the cell reinitiation.

The key to the high efficiency of the presented simulations is the generic implementation of the blockstructured AMR method after Berger and Collella [2] in the parallel AMROC framework [4]. AMROC provides the required high local resolution dynamically and distributes the AMR hierarchy at runtime. All presented results have been achieved on standard Linux-Beowulf-clusters of moderate size in a few days real time, which underlines the effectiveness of the approach.

References

- [1] J. Bell, M. Berger, J. Saltzman, and M. Welcome. Three-dimensional adaptive mesh refinement for hyperbolic conservation laws. *SIAM J. Sci. Comp.*, 15(1):127–138, 1994.
- [2] M. Berger and P. Colella. Local adaptive mesh refinement for shock hydrodynamics. *J. Comput. Phys.*, 82:64–84, 1988.
- [3] R. Deiterding. *Parallel adaptive simulation of multi-dimensional detonation structures*. PhD thesis, Techn. Univ. Cottbus, Sep 2003.
- [4] R. Deiterding. AMROC - Blockstructured Adaptive Mesh Refinement in Object-oriented C++. Available at <http://amroc.sourceforge.net>, Oct 2003.
- [5] Y. N. Denisov and Y. K. Troshin. Structura gazovoi detonatsii v trubakh (Structure of gaseous detonations in tubes). *Zh. Eksp. Teor. Fiz.*, 30(4):450–459, 1960.
- [6] C. A. Eckett. *Numerical and analytical studies of the dynamics of gaseous detonations*. PhD thesis, California Institute of Technology, Pasadena, California, Sep 2001.
- [7] B. Einfeldt, C. D. Munz, P. L. Roe, and B. Sjögreen. On Godunov-type methods near low densities. *J. Comput. Phys.*, 92:273–295, 1991.
- [8] W. Fickett and W. C. Davis. *Detonation*. University of California Press, Berkeley and Los Angeles, California, 1979.
- [9] T. Geßner. *Dynamic mesh adaption for supersonic combustion waves modeled with detailed reaction mechanisms*. PhD thesis, Math. Fakultät, University Freiburg, 2001.

- [10] B. Grossmann and P. Cinella. Flux-split algorithms for flows with non-equilibrium chemistry and vibrational relaxation. *J. Comput. Phys.*, 88:131–168, 1990.
- [11] M. Hanana, M. H. Lefebvre, and P. J. Van Tiggelen. Pressure profiles in detonation cells with rectangular or diagonal structure. In *Proc. of 17th Int. Colloquium on the Dynamics of Explosive and Reactive Systems*, Heidelberg, Jul 1999.
- [12] N. N. Janenko. *Die Zwischenschrittmethode zur Lösung mehrdimensionaler Probleme der mathematischen Physik*. Springer-Verlag, Berlin, 1969.
- [13] K. Kailasanath, E. S. Oran, J. P. Boris, and T. R. Young. Determination of detonation cell size and the role of transverse waves in two-dimensional detonations. *J. Combustion Flame*, 61:199–209, 1985.
- [14] P. Kaps and P. Rentrop. Generalized Runge-Kutta methods of order four with stepsize control for stiff ordinary differential equations. *Num. Math.*, 33:55–68, 1979.
- [15] R. J. Kee, F. M. Rupley, and J. A. Miller. *Chemkin-II: A Fortran chemical kinetics package for the analysis of gas-phase chemical kinetics*. SAND89-8009, Sandia National Laboratories, Livermore, California, Sep 1989.
- [16] R. J. Kee, F. M. Rupley, and J. A. Miller. *The Chemkin thermodynamic data base*. SAND87-8215B, Sandia National Laboratories, Livermore, California, Mar 1990.
- [17] B. Larrouturou. How to preserve the mass fractions positivity when computing compressible multi-component flows. *J. Comput. Phys.*, 95:59–84, 1991.
- [18] J. H. S. Lee. Dynamic parameters of gaseous detonations. *Ann. Rev. Fluid Mech.*, 16:311–336, 1984.
- [19] M. H. Lefebvre and E. S. Oran. Analysis of the shock structures in a regular detonation. *Shock Waves*, 4:277–283, 1995.
- [20] M. H. Lefebvre, E. S. Oran, K. Kailasanath, and P. J. van Tiggelen. The influence of the heat capacity and diluent on detonation structure. *J. Combustion Flame*, 95:206–218, 1993.
- [21] M. H. Lefebvre, E. S. Oran, K. Kailasanath, and P. J. van Tiggelen. Simulation of cellular structure in a detonation wave. *Prog. Astronaut. Aeronaut.*, 153:64–77, 1993.
- [22] E. S. Oran, J. W. Weber, E. I. Stefaniw, M. H. Lefebvre, and J. D. Anderson. A numerical study of a two-dimensional H₂-O₂-Ar detonation using a detailed chemical reaction model. *J. Combustion Flame*, 113:147–163, 1998.
- [23] J. J. Quirk. Godunov-type schemes applied to detonation flows. In J. Buckmaster, editor, *Combustion in high-speed flows: Proc. of a Workshop on Combustion, Oct 12-14, 1992, Hampton,*, pages 575–596, Dordrecht, 1994. Kluwer Acad. Publ.
- [24] R. Sanders, E. Morano, and M.-C. Druguet. Multidimensional dissipation for upwind schemes: Stability and applications to gas dynamics. *J. Comput. Phys.*, 145:511–537, 1998.
- [25] R. A. Strehlow. Gas phase detonations: Recent developments. *J. Combustion Flame*, 12(2):81–101, 1968.
- [26] R. A. Strehlow and F. D. Fernandez. Transverse waves in detonations. *J. Combustion Flame*, 9:109–119, 1965.
- [27] D. R. Stull and H. Prophet. JANAF thermodynamical tables. Technical report, U. S. Department of Commerce, 1971.
- [28] S. Taki and T. Fujiwara. In *18th Int. Symposium on Combustion*, pages 1671–1681, Pittsburgh, 1981. The Combustion Institute.
- [29] E. F. Toro. *Riemann solvers and numerical methods for fluid dynamics*. Springer-Verlag, Berlin, Heidelberg, 2nd edition, 1999.
- [30] B. van Leer. Towards the ultimate conservative difference scheme V. A second order sequel to Godunov’s method. *J. Comput. Phys.*, 32:101–136, 1979.
- [31] C. K. Westbrook. Chemical kinetics of hydrocarbon oxidation in gaseous detonations. *J. Combustion Flame*, 46:191–210, 1982.
- [32] D. N. Williams, L. Bauwens, and E. S. Oran. Detailed structure and propagation of three-dimensional detonations. In *26th International Symposium on Combustion*, Naples, Apr. 1996.
- [33] F. A. Williams. *Combustion theory*. Addison-Wesley, Reading, Massachusetts, 1985.

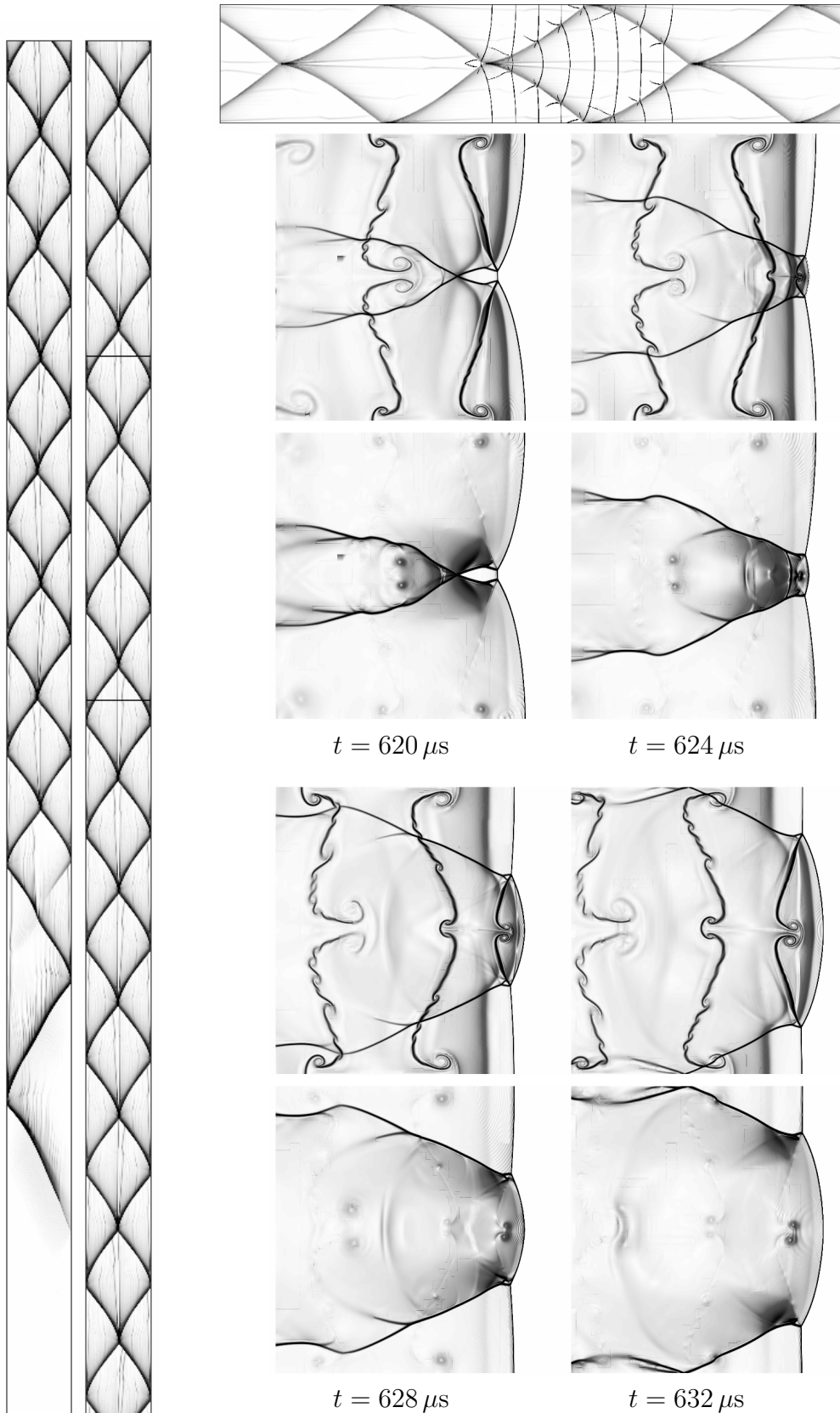
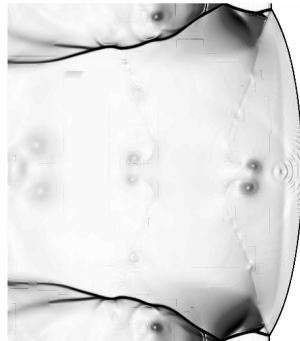
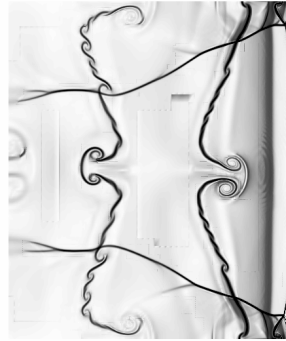
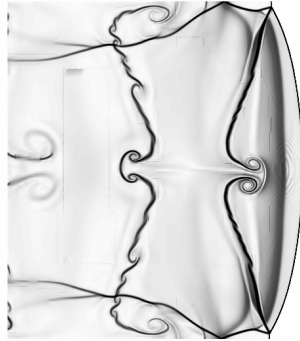
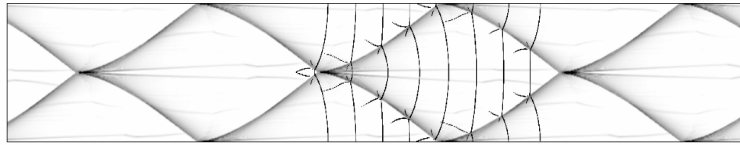
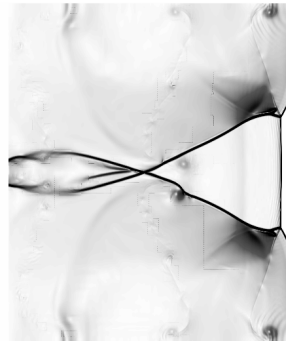
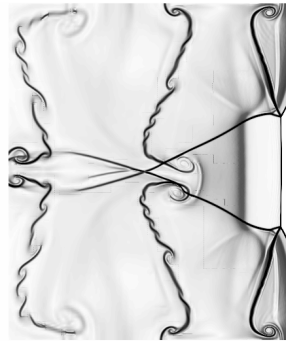
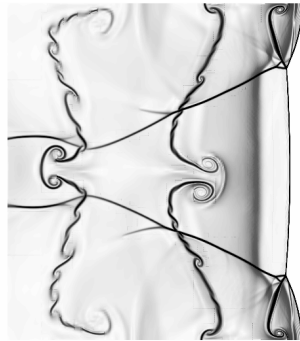


Figure 15: Triple point tracks and schlieren plots of T (upper graphic for each time step) and p (lower graphic) for the reinitiation and for the first half of a detonation cell, $44.8 \text{ Pts}/l_{ig}$.



$t = 636 \mu s$

$t = 640 \mu s$



$t = 644 \mu s$

$t = 648 \mu s$

Figure 16: Schlieren plots of T (upper graphic for each time step) and p (lower graphic) for the second half of a detonation cell, $44.8 \text{ Pts}/l_{ig}$.

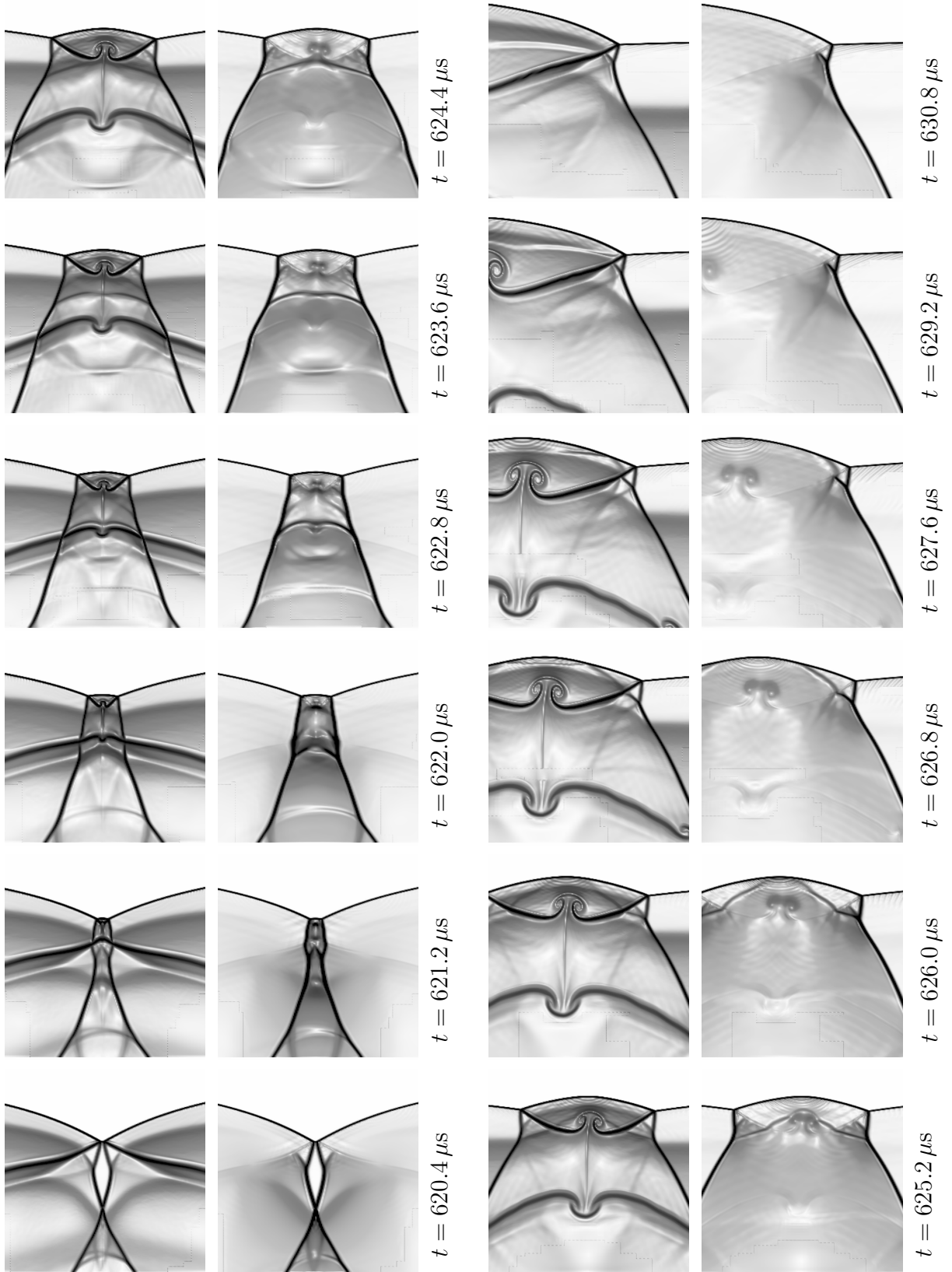


Figure 17: Schlieren plots T (upper graphic for each time step) and p (lower graphic) of the reinitiation process at the end of an old and at the beginning of a new detonation cell $44.8 \text{ Pts}/l_{ig}$.

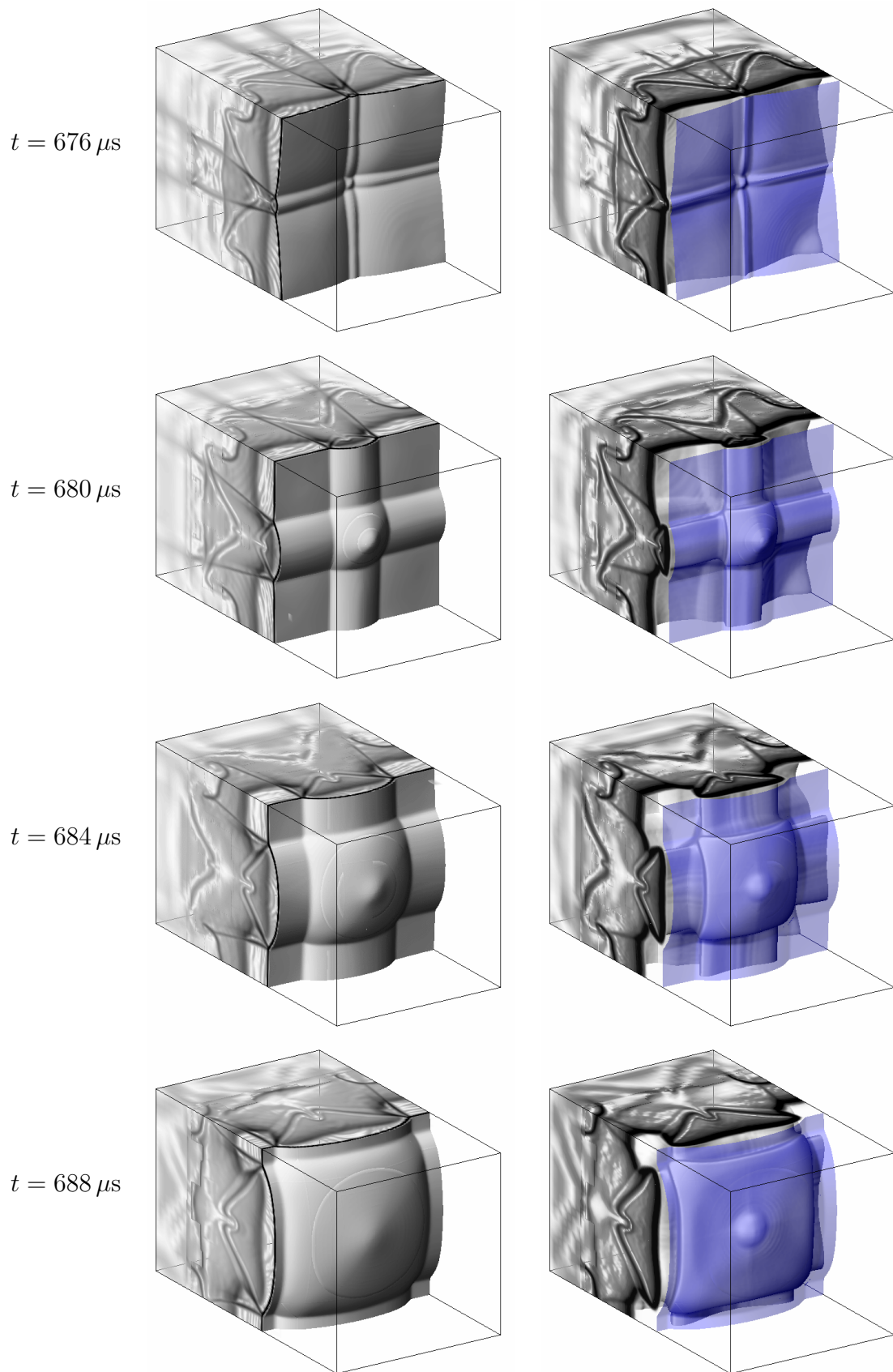


Figure 18: Schlieren plots of ρ (left) and Y_{OH} (right) in the first half of a detonation cell, mirrored at $x_2 = 0$ cm, $5.0 \text{ cm} < x_1 < 7.0 \text{ cm}$.

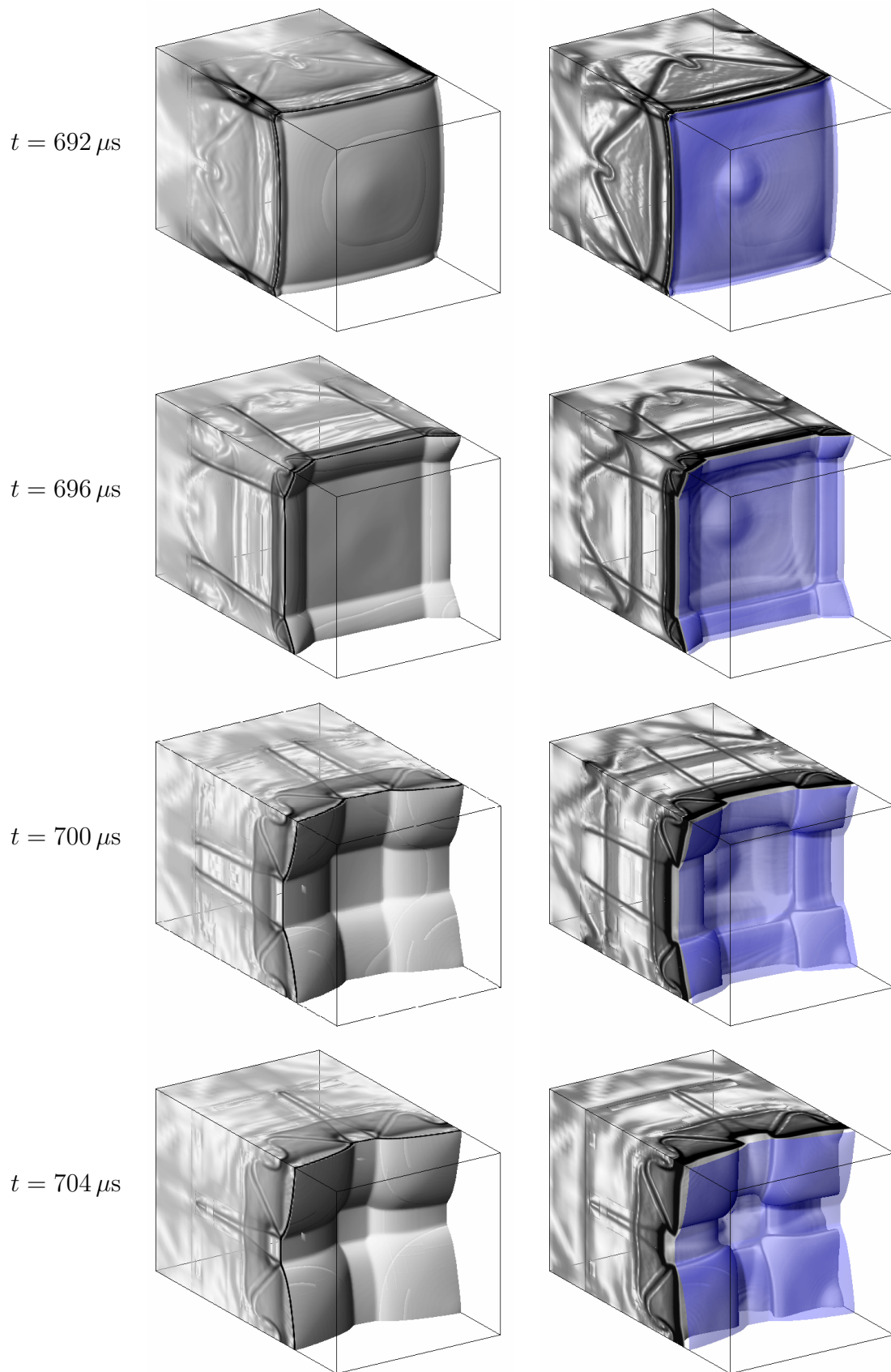


Figure 19: Schlieren plots of ρ (left) and Y_{OH} (right) in the second half of a detonation cell, mirrored at $x_2 = 0$ cm, $5.0 \text{ cm} < x_1 < 7.0$ cm.